Editors' Suggestion

Phonon dispersion in MoS_2

Hans Tornatzky,[1,*] Roland Gillen,[2] Hiroshi Uchiyama,[3] and Janina Maultzsch[2,†]

[1]*Institut für Festkörperphysik, Technische Universität Berlin Hardenbergstr. 36, 10623 Berlin, Germany*

[2]*Department Physik, Friedrich-Alexander-Universität Erlangen-Nürnberg, Staudtstr. 7, 91058 Erlangen, Germany*

[3]*Japan Synchrotron Radiation Research Institute (JASRI/SPring-8), 1-1-1 Kouto, Sayo, Hyogo 679-5198 Japan*

(Received 15 November 2018; revised manuscript received 1 April 2019; published 24 April 2019)

We present the phonon dispersion of bulk MoS_2 in the high-symmetry directions of the Brillouin zone, determined by inelastic x-ray scattering. Our results underline the two-dimensional nature of MoS_2. In combination with state-of-the-art first-principles calculations, we determine the phonon displacement patterns, symmetry properties, and scattering intensities. The results will be the basis for future experimental and theoretical work regarding electron-phonon interactions, intervalley scattering, as well as phonons in related 2D materials.

DOI: 10.1103/PhysRevB.99.144309

I. INTRODUCTION

Lattice dynamics constitute one of the most fundamental properties of a crystal, being the basis for mechanical and elastic properties, thermal transport as well as charge-carrier dynamics, phonon-assisted optical excitations, and many more. In this view, it is highly desired to have reliable data about the phonon dispersion relation of MoS_2, a layered crystal that has boosted the new research field of two-dimensional (2D) materials beyond graphene during recent years [1–5]. This is due to its fascinating physical properties in single-layer form, which it shares with related transition-metal dichalcogenides (TMDCs) like $MoSe_2$, WS_2, WSe_2, or $MoTe_2$ [6–9].

Many of their physical processes relevant for new applications [10,11], such as carrier and exciton dynamics [12–14], decay of so-called valley polarization [15–18] (the selective population of one of the two inequivalent K points in the Brillouin zone), and relaxation of spins [19,20], crucially depend on phonons. For example, phonons with considerably large wave vector are required for optical absorption and emission from the indirect band gap in few-layer and bulk TMDCs. They are the relevant source for electron scattering in electron transport [21] and are expected to play a significant role in the formation of momentum-space indirect interlayer excitons in van-der-Waals heterostructures [22,23].

In MoS_2 and other TMDCs, however, experimental data on the full phonon dispersion are missing. Only one high-symmetry direction of the Brillouin zone in MoS_2 has been accessed so far by inelastic neutron scattering (INS) [24]. However, the part most relevant for scattering with large phonon wave vectors q or between the inequivalent points K and K' (i.e., between the valleys) is completely missing and has been addressed by DFT calculations only so far, e.g., in Refs. [25–27]. This is compounded by the dependence of the phonon frequencies on the employed exchange-correlation approximation, raising the question of the accuracy of theoretical predictions for $q \neq 0$. The same holds for the other TMDCs, which have in common, as an obstacle for INS experiments, the in-plane nature of the phonon dispersion and the lack of large single crystals.

Here we present the entire phonon dispersion relation of MoS_2 in the high-symmetry directions Γ-K, Γ-M, K-M, and Γ-A of the Brillouin zone as determined by inelastic x-ray scattering (IXS) experiments. We show the existence of almost degenerate Davydov pairs throughout the Brillouin zone, as well as nearly quadratic dispersion of the out-of-plane acoustic modes (flexural modes), underlining the two-dimensional nature of MoS_2. We further present density-functional theory (DFT) calculations with implemented van-der-Waals correction and simulations of the structure factor, which determines the scattering intensities. They are in excellent agreement with the experimental data and reveal the mixing of in-plane and out-of-plane phonon displacement directions inside the Brillouin zone.

II. METHODS

A. Experimental setup

Our inelastic x-ray spectra were recorded at beamline 35XU at the SPring-8 (Japan). A beam with a photon energy of 17.7935 keV with a spectral width of $\lesssim$3 meV (full width of half maximum, FWHM) was obtained by using a liquid-nitrogen cooled Si (111) high heat load premonochromator, reducing the FWHM to $\approx$1 eV. The final width was created with a near-backscattering main monochromator of which the Si (999) reflex was used. The beam was then focused onto the sample with a spot size of $75 \times 63 \mu m^2$, enabling us to select a single crystalline domain of the bulk MoS_2 crystal. The scattered photons were analyzed by an array of 3×4 bent Si (111) analyzers, attached to the 10 m monochromator arm. A detailed description of the beamline can be found in Ref. [28].

The measurements were performed by keeping the scattering wave vector Q (and thereby the phonon wave vector

*ht07@physik.tu-berlin.de
†janina.maultzsch@fau.de

 ©2019 American Physical Society

q) constant and scan the energy by varying the temperature of the backscattering main monochromator. The twelve analyzers were kept at a fixed energy (i.e., temperature). To verify that no significant energy shifts of analyzers and main monochromator have occurred, Stokes-anti-Stokes pairs of inelastically scattered photons were measured between most of the energy scans. The measurements were performed in reflection geometry for ΓA longitudinal and all out-of-plane transverse modes and in transmission for ΓM, ΓK, and KM longitudinal and in-plane transverse modes. To record signal from low-intensity modes, momentum resolution was set to 0.75 nm^{-1}.

The sample is a synthesized crystal (HQ graphene, Netherlands) with a thickness of about 150 μm to match the attenuation length of the used x rays in MoS_2, yielding the best tradeoff between high absorption and low scattering in a transmission setup. All measurements were taken in ambient conditions.

B. Computational approach

We calculated the theoretical phonon band structure within the frame of density functional perturbation theory (DFPT) on the level of the generalized gradient approximation in the Perdew-Burke-Ernzerhof flavor [29] (GGA-PBE) as implemented into the QUANTUM ESPRESSO suite [30]. Long-range noncovalent interactions were included through the semiempirical DFT-D3 correction with Becke-Johnson damping [31],

$$E^{D3} = \frac{1}{2}\sum_{A}\sum_{B}\left(C_6^{AB}\frac{s_6}{R_{AB}^6 + f^6} + C_8^{AB}\frac{s_8}{R_{AB}^8 + f^8}\right),$$

where R_{AB} is the distance between atom A in a central unit cell and atom B in the crystal. We included all atoms within a cutoff distance of 100 Å from the center of the central unit cell in the sum over B. C_n^{AB} is the nth order dispersion coefficient for the pair of atoms A and B. $f = a_1 R_{AB}^0 + a_2$ is a damping constant, with a 'covalent distance' $R_{AB}^0 = \sqrt{C_8^{AB}/C_6^{AB}}$ [31]. Here, we used our own set of parameters ($s_6 = 1.0$, $s_8 = 0.9184$, $a_1 = 0.5484$, $a_2 = 2.156$ Å), which was fitted to reproduce the experimental lattice constants of a wide variety of layered and bulk materials and had been used previously [22,32,33] with great success. The Mo($3s$, $3p$, $3d$, $4s$) and the S($3s$, $3p$) states were treated as valence electrons using multiprojector optimized normconserving Vanderbildt (ONCV) pseudopotentials [34,35] with a cutoff of 120 Ry. All reciprocal space integrations were performed by a discrete q point sampling of $12 \times 12 \times 4$ q points in the Brillouin zone. We fully optimized the atomic positions and cell parameters until the residual forces between atoms and the cell stress were smaller than 0.001 eV/Å and 0.01 GPa, respectively. The threshold for the total energy was set to 10^{-14} Ry, which ensured tightly converged interatomic forces for the geometry optimization and of the ground state density and wave functions for the DFPT calculations. The phonon band structure was obtained through Fourier interpolation using the explicitly calculated phonon frequencies on a regular grid of $12 \times 12 \times 4$ q points. The contributions to the dynamical matrix from the D3 corrections were fully included in the phonon calculations.

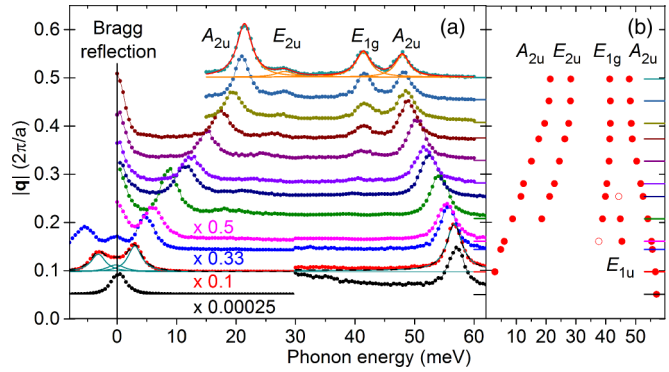

FIG. 1. (a) Experimental IXS spectra of MoS_2 along the Γ-M direction (in the vicinity of the (0 0 12) Bragg reflection) with vertical offsets corresponding to the phonon q vector. The four spectra closest to Γ are scaled by the factor given next to the spectrum. (b) Extracted peak positions of the spectra shown in (a). Peaks are labeled according to their symmetry and notation at the Γ point.

III. RESULTS AND DISCUSSION

2H-MoS_2 forms a hexagonal crystal with space group $P6_3/mmc$ (D_{6h}^4 in Schönfließ notation) with six atoms in the unit cell, giving rise to 18 phonon branches. At the Γ point, the phonon modes decompose into the irreducible representations

$$\Gamma_{2H} = A_{1g} \oplus 2A_{2u} \oplus 2B_{2g} \oplus B_{1u} \oplus E_{1g} \oplus 2E_{1u} \oplus 2E_{2g} \oplus E_{2u}$$

for the conventional definition of a 120° angle between the in-plane lattice vectors [38,39]. Due to the relatively weak noncovalent coupling of the MoS_2 layers, the phonon branches are nearly doubly degenerate at almost all q vectors in the Brillouin zone and correspond to the nine phonon branches of single-layer MoS_2 (three atoms per unit cell, space group $P\bar{6}m2$, D_{3h}).

In Fig. 1(a), a selection of the measured IXS spectra is plotted. The displayed spectra were measured along (0 0+q 12), with the absolute value of the phonon wave vector $|\mathbf{q}| = q = 0 \ldots 0.5$ in units of the reciprocal lattice vector. Here, (h k l) are the Miller indices identifying the scattering vector of the elastically scattered light, i.e., a Bragg peak. The extracted peak positions thus represent the dispersion of the out-of-plane transverse modes from Γ to M, see Fig. 1(b).

The IXS measurements allowed us to identify all acoustic and almost all optical phonon branches along the A-Γ-K-M-Γ directions as shown in Fig. 2. IXS data are shown by circles together with theoretical values from DFT calculations (lines). Phonon energies obtained by Raman spectroscopy of the same sample (stars in Fig. 2) complement the IXS results with data at the Γ point. We find seamless agreement between the Γ-point frequencies and the IXS data.

In the experiment, we observe nine phonon branches. The calculations show that they are almost doubly degenerate,

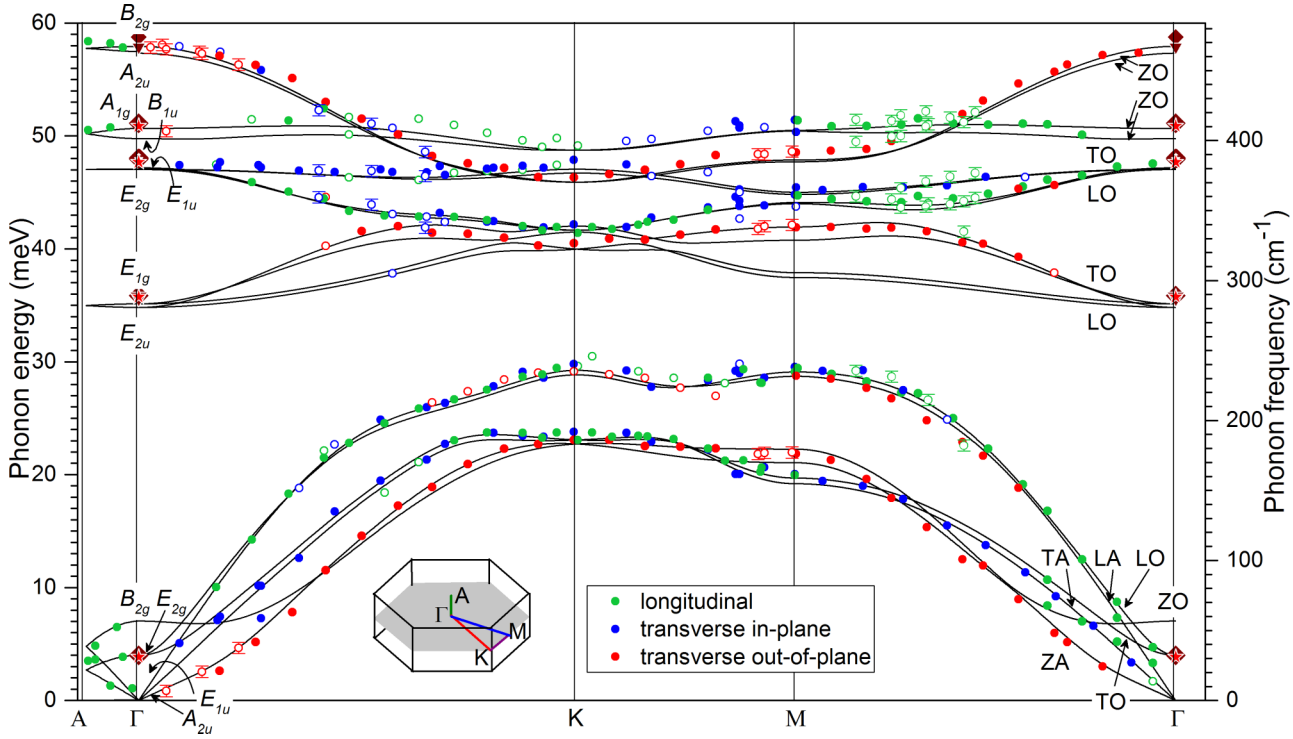

FIG. 2. Inelastic x-ray scattering measurements and density-functional perturbation theory calculations of the phonon dispersion of MoS_2 along the high-symmetry directions A-Γ-K-M-Γ. Circles in green/blue/red represent measurements probing phonons with an in-plane longitudinal (L)/in-plane transverse (T)/out-of-plane transverse (Z) component. For symbols without an error bar, the error is estimated to be smaller than the symbol size. Open symbols depict peaks with small intensities or larger error. Values at the Γ point are Raman and IR spectroscopy data from the literature [36–38] (diamonds) and from Raman measurements on the same sample as used in the IXS experiment (stars). Phonon branches are labeled by their symmetry within the D_{6h} at the Γ point, as well as by their displacement (L, T, Z) and acoustic (A) or optical (O) character. For a symmetry labeling at the K and M points, see Table I; for a compilation of the eigenvectors see Appendix B.

as expected from the weak interlayer forces. The energy resolution in the IXS experiment, however, does not allow us to distinguish these so-called Davydov pairs: Each pair is formed by two phonon modes, where the two layers forming the bulk unit cell (i) have both the same displacement pattern as the single layer and (ii) the displacement of one of the layers is shifted in phase by π. At the Γ point, one of the bulk modes of such a pair is always even with respect to spatial inversion and the other one is odd [36,38]. The frequency difference of the two phonons in a Davydov pair is very small if the interaction between the layers is weak. Only the acoustic phonons have fundamentally different behavior: One mode is still acoustic (zero frequency), whereas the other one has finite frequency and corresponds to a rigid-layer vibration at the Γ point.

Near the Γ point, the phonon modes have well defined displacement direction, i.e., in-plane longitudinal (L), in-plane transverse (T), and out-of-plane transverse (Z). This is seen by the color of the symbols representing the IXS data, which indicates the displacement direction preferentially detected in the given scattering geometry. Towards the K and M points, we observe data points with different colors (i.e., different preferred displacement directions) on the same branch, see for instance the longitudinal acoustic (LA) branch. We interpret this by an increased mixing of the displacement directions for increasing q. This is supported by our calculations of the phonon eigenvectors, see Fig. 3 for the example of the transverse E_{1g} branch and Tables II–IV in Appendix B for a compilation of all 18 eigenvectors at the Γ, K, and M points. Note that the mixing is not limited to the in-plane direction but includes the out-of-plane modes as well, in contrast to the example of graphite [40]. This mixing also explains why some of the phonon branches are only partially observed or show weak signal: For instance, the phonon branch with E_{1g} symmetry at the Γ point (in-plane vibration) cannot be observed in the chosen scattering geometry (see also discussion below). However, it gains an out-of-plane component for $q > 0$, see Fig. 3, which results in (weak) IXS signal. Furthermore, we observe a quadratic dispersion of the ZA branch (also called flexural mode) near the Γ point, which is typical for

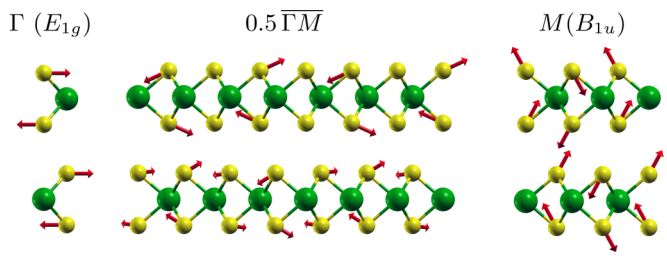

FIG. 3. Transition of the phonon eigenvectors from the Γ to the M point of the branch with E_{1g} (TO) symmetry at the Γ point. Appendix B for a complete overview of the phonon eigenvectors at the Γ, K, and M points.

TABLE I. Phonon frequencies (given in cm^{-1}) of MoS_2 at the Γ, K, and M high-symmetry points from our DFT calculations and experiments (Raman and IR spectroscopy at Γ and IXS at K, M). n.a. – identifies not active phonon modes in Raman and IR experiments. The phonon modes are labeled by their irreducible representations in the factor groups D_{6h} (Γ), D_{3h} (K), and D_{2h} (M). For a group theory analysis of phonons in MoS_2, see also Ref. [39]. Lines connect phonons that belong to the same phonon branch.

Γ (space group D^4_{6h})					**K** (D^4_{3h})			**M** (D^{17}_{2h})			**Γ**	
irr. rep.		Raman	IR	DFT	irr. rep.	IXS	DFT	irr. rep.	IXS	DFT	irr. rep.	
E_{1u}	TA	n.a.	→0	0.0	E''	186	183.1	B_{1g}	161	154.7	E_{1u}	TA
	LA							B_{2u}		158.7		LA
A_{2u}	ZA				E'	189	186.0	B_{1u}	176	169.7	A_{2u}	ZA
E_{2g}	TO	31 – 32[a] [37]		32.2				B_{2g}		179.4	E_{2g}	TO
	LO				A'_2	239	232.5	A_g	235	231.5		LO
B_{2g}	ZO	n.a.		56.6	A'_1		235.8	B_{3u}		234.6	B_{2g}	ZO
E_{2u}	LO		n.a.	280.7	E''	327	322.3	B_{3g}		302.1	E_{2u}	LO
	TO							A_u		305.5		TO
E_{1g}	LO	286 – 289[b] [36,37]		283.3	A''_2	334	334.5	B_{2g}		328.7	E_{1g}	LO
	TO				E'	334	335.9	B_{1u}	338	338.1		TO
E_{2g}	LO	383 – 384[b] [36,37]		379.2				A_g	353	354.8	E_{2g}	LO
	TO				A''_1	340	339.0	B_{3u}		355.6		TO
E_{1u}	LO	n.a.	384 [36]	379.4	E''	373	370.1	B_{1g}	361	361.4	E_{1u}	LO
	TO			380.4				B_{2u}	364	362.9		TO
B_{1u}	ZO		n.a.	401.3	A'_2	384	376.7	B_{1u}	392	384.7	B_{1u}	ZO
A_{1g}	ZO	408 – 410[b] [36,37]		408.5	A'_1		379.4	B_{2g}		386.0	A_{1g}	ZO
A_{2u}	ZO	n.a.	470 [36]	462.2	E'	398	393.0	A_g	410	406.6	A_{2u}	ZO
B_{2g}	ZO		n.a.	467.1				B_{3u}		407.1	B_{2g}	ZO

[a]Measured with 633 nm excitation.
[b]Measured with 457 nm excitation.

two-dimensional atomically thin sheets [41] and underlines the 2D nature of the MoS_2 layers even within the bulk crystal.

One challenge for lattice-dynamics simulations in layered materials is the proper description of the effect of noncovalent interactions, which bind the individual layers together. This is particularly relevant for the rigid-layer, low-frequency shear, and breathinglike modes in the vicinity of the Γ point, where the force constants are small and dominated by contributions from the noncovalent interlayer coupling. The commonly used local density approximation (LDA) to DFT appears to offer a consistently good agreement with experimental phonon frequencies for a wide range of layered and bulk crystals but largely benefits from its intrinsic overbinding, which causes a hardening of the predicted phonons at the cost of significantly lower-quality lattice constants.

Therefore, we implemented the contributions from the popular DFT-D3 van-der-Waals corrections [31] to the dynamical matrix [42] to the density functional perturbation theory code in the QUANTUM ESPRESSO package [30]. These semiempirical corrections introduce an additional attractive London-like interatomic potential, which compensates for the underbinding and intrinsic exponential decay of nonclassical interactions in the GGA-PBE exchange-correlation approximation [29] we used for our computations. The obtained lattice constants of $a = 3.158$ Å and $c = 12.229$ Å from our PBE+D3 calculations are close to the lattice constants of our MoS_2 sample of $a^{exp} = 3.161$ Å and $c^{exp} = 12.297$ Å, suggesting a convincing description of both covalent and noncovalent interatomic bonding in MoS_2, in agreement with previous studies [22,32,33].

The inclusion of noncovalent interactions leads to a noticeable improvement for the values of the low-frequency modes close to the Γ point, which are significantly underestimated in the GGA-PBE approximation without the D3 correction (not shown). Our calculated phonon dispersion is in excellent quantitative agreement with the IXS measurements for the acoustic and low-energy optical modes (Table I) and correctly describes the small 'bumps' in the dispersion of the Davydov pair of the LA-derived branch [E_{2g} (LO, shear mode) and E_{1u} (LA) at the Γ point] along Γ-K-M-Γ, see Fig. 2.

We find a small overestimation of our predicted frequencies of the out-of-plane acoustic (ZA) mode compared to the IXS measurements. While the deviation is within the margin of error in our measurements, we note that this mode is particularly difficult to converge with the cutoff energy of the plane-wave expansion that we use in our calculations, due to the weak forces between the rigidly oscillating layers. This situation is similar to the ZA modes in graphite and layered boron nitride.

For the higher-frequency modes, our PBE+D3 approach appears to perform slightly less well compared to the Raman measurements and the local-density approximation

results from Ref. [26], and systematically underestimates the frequencies of the Raman active modes by a few cm^{-1}, see Table I. In general, the predictions from LDA calculations are somewhat higher than those from our PBE+D3 calculations, hence leading to a slightly better agreement between theory and the Raman and IXS measurements for the high-energy optical modes compared to PBE+D3 calculations, while the agreement for the acoustic and low-energy optical modes is worse. The good quality predictions of the optical modes appears to be consistent for a wide range of layered crystals but is to a certain extent fortuitous due the intrinsic overbinding of LDA causing a hardening of the predicted phonons at the cost of significantly lower-quality lattice constants. The DFT-D3 method hence simultaneously offers an accurate description of both vibronic and structural properties of layered MoS_2 that goes beyond the capabilities of noncorrected local DFT approximations such as LDA, PBE, or PBEsol [43].

An improved quantitative agreement over the full frequency range of MoS_2 and similar layered materials hence requires an exchange-correlation approximation that predicts a stronger (weaker) in-plane covalent bonding than PBE (LDA) and sufficiently soft interlayer noncovalent interaction. Due to the generally attractive nature of the DFT-D3 corrections, a good description of both structural and vibronic properties would then require an exchange-correlation functional that slightly overestimates both in-plane and out-of-plane lattice constants. An alternative to semiempirical dispersion corrections might be an approach based on nonlocal van-der-Waals correlation functionals from the vdW-DF [44,45] or the VV10 [46] families that are combined with the PBEsol functional or similar approximations, which are well suited for the description of lattice constants in extended systems.

While we observed the phonon dispersion of eight of the nine Davydov pairs in the experiment, we were unable to access the almost degenerate branches derived from the two LO modes around 35 meV (E_{2u} and E_{1g} at the Γ point) in the Γ-K and Γ-M directions in our scattering geometries. In order to understand this, we simulated the dynamical structure factor [47,48] using data from our DFT calculations, see Appendix A for details. The simulations suggest that destructive interference of the counterphase oscillation of the sulfur sublayers in each MoS_2 layer cause extinction of the structure factor for all q vectors along the Γ-M and Γ-K-M directions, if a Bragg peak ($h\,k\,0$) is used.

Using a Bragg peak ($h\,k\,l$) with a suitable out-of-plane component $l \neq 0$ should lead to activation of the LO E_{1g} and E_{2u} branches, caused by symmetry breaking of the phase factors from the atomic positions, which lifts the destructive interference. The intensity can be enhanced through a wise choice of the Bragg peak such that it aligns the signs of the contributions from the atomic displacements and of the phase factors from the atomic positions. This is illustrated in Fig. 4(a) for simulated measurements at the Bragg peak (−2 4 2) in the direction (q 0 0). Further, our simulations correctly reproduce the deactivation of the transverse E_{2u} branch and activation of the longitudinal E_{1g} branch in the vicinity of the K point that we observed in our IXS experiments near the (0 0 12) peak, see Fig. 4(b). This arises from a change of atomic displacement patterns of the longitudinal E_{2u} and E_{1g} modes from a pure in-plane to a pure out-of-plane nature

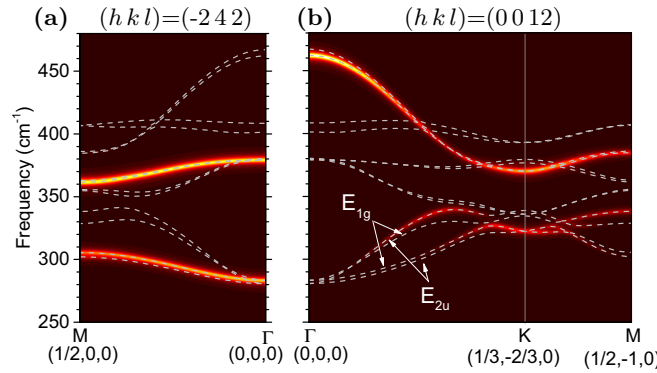

FIG. 4. (a) Simulated dynamical structure factor illustrating the possible observation of the branches associated to the longitudinal E_{1g}/E_{2u} modes at the (−2 4 2) Bragg peak. (b) Simulation used for the assignment of the measured out-of-plane phonon energies at the (0 0 12) Bragg peak, showing the emergence of significant scattering cross section for the longitudinal E_{1g}/E_{2u} branches around K.

close to the K point, such that these modes behave similarly to the ZO modes. On the other hand, the transverse E_{2u} and E_{1g} modes adopt a mixed out-of-plane/in-plane nature in the middle of the Γ-K and Γ-M lines [thus coupling to the (0 0 12) Bragg peak] but revert back to a pure in-plane character in the vicinity of the K point, see Table III in Appendix B.

An overview of the measured phonon frequencies, compared to Raman and IR spectroscopy data at the Γ point and to DFT calculation at the Γ, K, and M points, is given in Table I. A detailed comparison of our IXS data with measurements performed by electron energy loss spectroscopy (EELS) [49] and inelastic neutron scattering (INS) [24] are given in the Supplemental Material [50].

IV. CONCLUSIONS

In conclusion, the complete phonon dispersion relation of MoS_2 is determined experimentally in the high-symmetry directions of the Brillouin zone. In combination with DFT calculations, the data clearly show the 2D character of the lattice vibrations in this layered crystal. Therefore, the results are relevant for the monolayer form of MoS_2 and isostructural TMDCs as well. In particular, the understanding of scattering processes involving phonons, such as in electron transport or optical transitions involving the indirect band gap or the two K valleys, will in future be based on the knowledge of the phonon dispersion relation.

ACKNOWLEDGMENTS

We thank Daniela Beiße, Marco Haupt, Andreas Ludewig, and Wolfgang Piper (TU Berlin) for the design and construction of the sample holder and Johannes Enslin (TU Berlin) for preparative XRD measurements. Computational resources used for the simulations were provided by the HPC of the Regional Computer Centre Erlangen (RRZE). This work was supported by the SPring-8 under proposal number 2017B1738 and by the Deutsche Forschungsgemeinschaft (DFG) within the Cluster of Excellence "Engineering of Advanced Materials" (project EXC 315) (Bridge Funding).

APPENDIX A: SIMULATION OF IXS INTENSITIES

To supplement our experimental data and obtain more insight into the observed relative scattering intensities, we simulated the dynamical structure factor of MoS_2 for inelastic x-ray (and neutron) scattering. Following Ref. [47], we compute the one-phonon contribution to the dynamical structure factor for a reduced phonon wave vector $\mathbf{q}$ through

$$S(\mathbf{q},\omega)_{hkl} \propto \sum_{j}^{3N_{\text{at}}} \left| \sum_{d} \frac{f_d(\mathbf{G}_{hkl}+\mathbf{q})}{\sqrt{2M_d}} e^{-W_d(\mathbf{G}_{hkl}+\mathbf{q})} (\mathbf{G}_{hkl}+\mathbf{q}) \cdot \mathbf{e}_{\mathbf{q}jd}\, e^{i(\mathbf{G}_{hkl}+\mathbf{q})\cdot\mathbf{x}_d} \right|^2 F^{\text{DHO}}_{\mathbf{q}j}(\omega), \tag{A1}$$

where $\mathbf{x}_d$ and M_d are the position and mass of atom d in the unit cell, respectively, $\mathbf{e}_{\mathbf{q}jd}$ is the displacement of atom d due to phonon mode j, and $\mathbf{G}_{hkl}$ is the reciprocal lattice vector corresponding to the Bragg peak ($h\ k\ l$). N_{at} is the number of atoms in the unit cell, e^{2W_d} is the Debye-Waller factor of atom d, while f_d is the wave-vector-dependent form factor and readily available in tabulated form.

We approximate the spectral shape and temperature dependence of the structure factor due to electron-phonon and phonon-phonon scattering by a damped harmonic oscillator (DHO) model [48]

$$F^{\text{DHO}}_{\mathbf{q}j}(\omega) = \frac{4\omega}{\pi(1-e^{\hbar\omega/k_BT})} \frac{\gamma_{\mathbf{q}j}}{\left(\omega^2-\Omega^2_{\mathbf{q}j}\right)^2+4\omega^2\gamma^2_{\mathbf{q}j}},$$

where $\omega_{\mathbf{q}j}$ and $\gamma_{\mathbf{q}j}$ are the angular frequency and linewidth of phonon mode j at wave vector $\mathbf{q}$, respectively. $\Omega^2_{\mathbf{q}j} = \omega^2_{\mathbf{q}} + \gamma^2_{\mathbf{q}j}$ is the effective frequency of the phonon mode. The Debye-Waller factor e^{2W_d} is potentially important in our case as it might be different for different atoms/species and cause further qualitative differences of the phonon modes, e.g., modes with smaller or larger oscillations of the molybdenum atoms, in terms of inelastic scattering of x rays. We thus explicitly included the Debye-Waller factor, with [47]

$$W_d(\mathbf{G}_{hkl}+\mathbf{q}) = \frac{\hbar}{4M_dN_q} \sum_{\mathbf{q}} \sum_{j}^{3N_{\text{at}}} \frac{1}{\omega_{\mathbf{q}j}} \left|(\mathbf{G}_{hkl}+\mathbf{q})\cdot\mathbf{e}_{\mathbf{q}jd}\right|^2 \cdot \coth\left(\frac{\hbar\omega_{\mathbf{q}j}}{2k_BT}\hbar\right), \tag{A2}$$

which requires a sum over N_q vectors in the first Brillouin zone of the crystal. We found a negligible qualitative dependence of our results on W_d. Frequencies and normalized eigenvectors of the phonon modes for the calculation of the dynamical structure factor were obtained from Fourier interpolation along the ΓKM and ΓM paths that we used in our IXS experiments. The integration over the first Brillouin zone in Eq. (A2) was performed over a regular grid of $30 \times 30 \times 6$ q points. The linewidth $\gamma_{\mathbf{q}j}$ could be derived *ab initio* from calculations of the contributions of electron-phonon and phonon-phonon coupling to the imaginary part of the phonon self-energy, for example using the EPW and D3 codes in the QUANTUM ESPRESSO package. However, for reasons of simplicity, we opted for using a value of 0.05 cm^{-1} in our calculations instead. The simulated dynamical structure factors for the longitudinal and transverse optical modes corresponding to our experimental setups are shown in Fig. 5.

In general, the simulated spectra are in good qualitative agreement with our experimental observations and explain the observed signals and relative intensities for the 12 included optical modes. In particular, our simulations correctly predict the branches associated to the longitudinal E_{2u} and E_{1g} modes at the Γ point around 35 meV to be inactive for most of the Γ-K and Γ-M directions in our experimental geometries [54]. This can be understood from the atomic displacement patterns in Tables II–IV. For these two branches, the two sulfur sublayers in each MoS_2 vibrate in opposite phase, causing destructive interference in Eq. (A1). For wave vectors with a vanishing out-of-plane component, i.e., $\mathbf{q} = (q_{g1}\ q_{g2}\ 0)$, the atomic displacements of the sulfur atoms remain perfectly in-plane for most of the Γ-K and Γ-M high-symmetry lines, and the contributions from the vibrating sulfur layers exactly cancel each other out. At the same time, the contributions to Eq. (A1) from the equilibrium atomic positions $\mathbf{x}_d$ are equal for all sulfur atoms in a MoS_2 layer for the out-of-plane component $q_z = 0$. The dynamical structure factor hence vanishes, explaining our observations. As the contributions to the structure factor within each MoS_2 layer cancel, this result does not depend on the relative movement (in-phase or counterphase) of the two MoS_2 layers that is the difference between the E_{2u} and E_{1g} modes at Γ. From our simulations, it also does not depend on the Bragg peak used in the measurements as long as the z component of the phonon wave vector is zero.

On the other hand, our DFT calculations suggest that the dispersion of the optical modes is very weak in the out-of-plane, i.e., Γ-A direction. This feature could be exploited in order to gain experimental access to the full dispersion of the longitudinal $E^{\Gamma}_{2u}/E^{\Gamma}_{1g}$ branches: A significant out-of-plane component of the wave vector should break the symmetry of the vibration of the two sulfur sublayers in each of the MoS_2 layers and lift the destructive interference. Alternatively, one could attempt to break the symmetry of the contributions $e^{i(\mathbf{G}_{hkl}+\mathbf{q})\cdot\mathbf{x}_d}$ in Eq. (A1) from the equilibrium positions of the sulfur atoms by scattering the x rays off lattice planes ($h\ k\ l$) with $l \neq 0$. Figure 6 shows the simulated dynamical structure factors for a selection of Bragg peaks in Γ-M and "Γ'-M'" (with an offset $q_z = \frac{1}{4}$) direction. In all cases, breaking of the sulfur sublayer symmetry activates the longitudinal E^{Γ}_{1g} or the longitudinal E^{Γ}_{2u}. The similarity of the results for $q_z = 0$ and $q_z = \frac{1}{4}$ suggest that the activation mainly arises from a symmetry breaking of the phase factors from the equilibrium atomic positions, while the contribution from symmetry breaking of the displacement patterns is comparatively small. Depending on the choice of Bragg peak used for IXS, the phase factors $e^{i(\mathbf{G}_{hkl}+\mathbf{q})\cdot\mathbf{x}_d}$ can cause destructive interference between the sulfur sublayers, hence lowering or even extinguishing the scattering intensity, or can cause constructive interference. A choice of Bragg peak that properly aligns the signs of the phase factors from the equilibrium atomic positions with the signs of the corresponding contributions from the atomic displacement, $(\mathbf{G}_{hkl}+\mathbf{q})\cdot\mathbf{e}_{\mathbf{q}jd}$, hence should make the longitudinal E_{2u} and E_{1g} branches

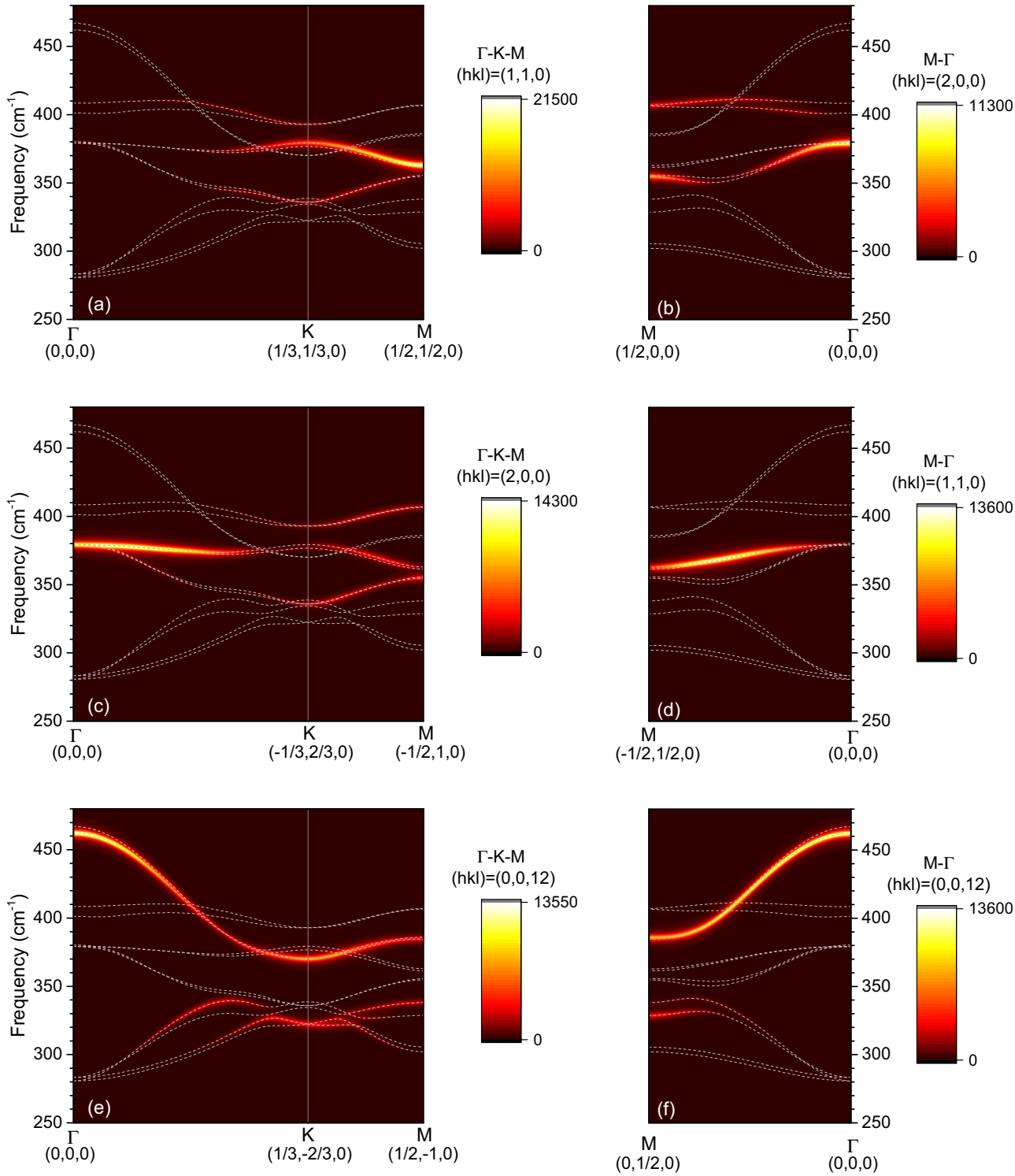

FIG. 5. Simulated dynamical structure factors for the Bragg peaks and paths in reciprocal space used in our IXS experiments. The phonon dispersion of the optical branches from our DFT calculations is shown as an overlay (dashed lines). The intensity is given in arbitrary units and is meaningful for comparison of the relative scattering intensity between the different experimental geometries.

experimentally accessible along the Γ-*K* and Γ-*M* paths in future experiments.

This approach is not necessary for the *transverse* E^{Γ}_{2u} and E^{Γ}_{1g} branches. For these modes, the displacements of the sulfur atoms gain a significant out-of-plane component for wave vectors away from the Γ point, which causes a natural symmetry breaking of the contributions from the atomic displacement patterns. The two modes hence behave similarly to the ZO modes and contribute to IXS for a Bragg peak with an out-of-plane component, in case of our

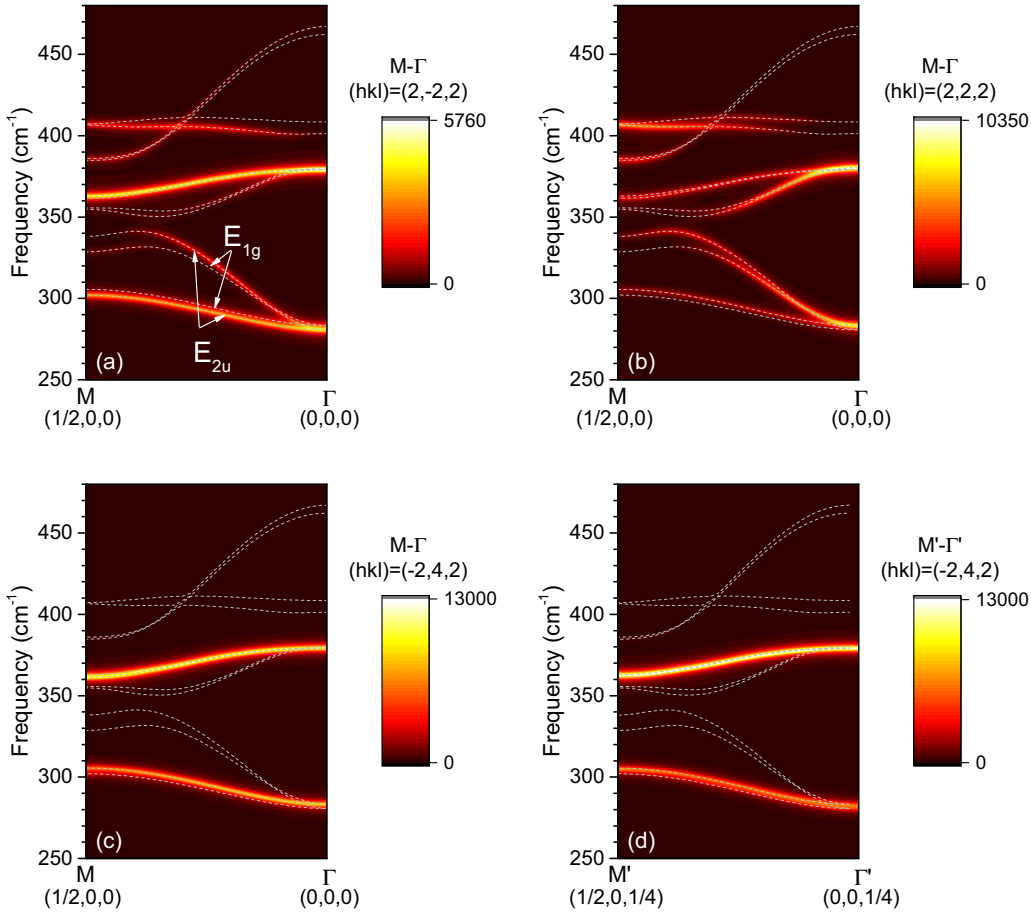

FIG. 6. Dynamical structure factors for a selection of experimental geometries that might yield scattering contributions from the Davydov pair of branches associated to the longitudinal E_{2u} and E_{1g} modes at the Γ point, which we did not observe in our experiments (except near the K point). The scattering intensity shows a strong qualitative and quantitative dependence of the chosen Bragg peak, while the effect of symmetry breaking through an out-of-plane offset of the phonon wave vectors is small.

experiments $(k\,k\,l) = (0\,0\,12)$. As our simulations suggest, $(k\,k\,l) = (2\,2\,2)$ or similar combinations of q_{g1} and q_{g2} suitable for transverse modes might work as well or even better along the Γ-K and Γ-M direction. The situation reverses in the vicinity of the K point: Here, the transverse E_{2u} and E_{1g} modes revert back to completely in-plane displacement patterns, while the longitudinal modes evolve into pure out-of-plane vibrations, see Table III. This causes an apparent crossing of the transverse and longitudinal E^{Γ}_{2u} and E^{Γ}_{1g} branches close to the K point in both IXS experiments and the simulated dynamical structure factor in Fig. 5(e). However, the calculated dispersion and the evolution of the atomic displacement patterns along the Γ-K path suggest that this apparent crossing is an actual anticrossing and that the scattering intensity is transferred from the (pseudo)transverse modes to the (pseudo)longitudinal modes in the vicinity of the K point.

APPENDIX B: DISPLACEMENT PATTERNS AT Γ, *K*, AND *M* HIGH-SYMMETRY POINTS

Tables II–IV depict a compilation of displacement patterns at the high-symmetry points Γ, K, and M, as derived from our DFT calculations. For each phonon the following information is given: the symmetry at the high-symmetry point and corresponding symmetry at the Γ point of the branch, along with its energy (in cm^{-1} and meV) and projections onto the planes depicted in the bottom right panel of Table II.

TABLE II. Phonon eigenvectors of MoS_2 at the Γ point. Frames surround Davydov pairs. For each phonon the projections onto the planes depicted in the panel on the bottom right are shown.

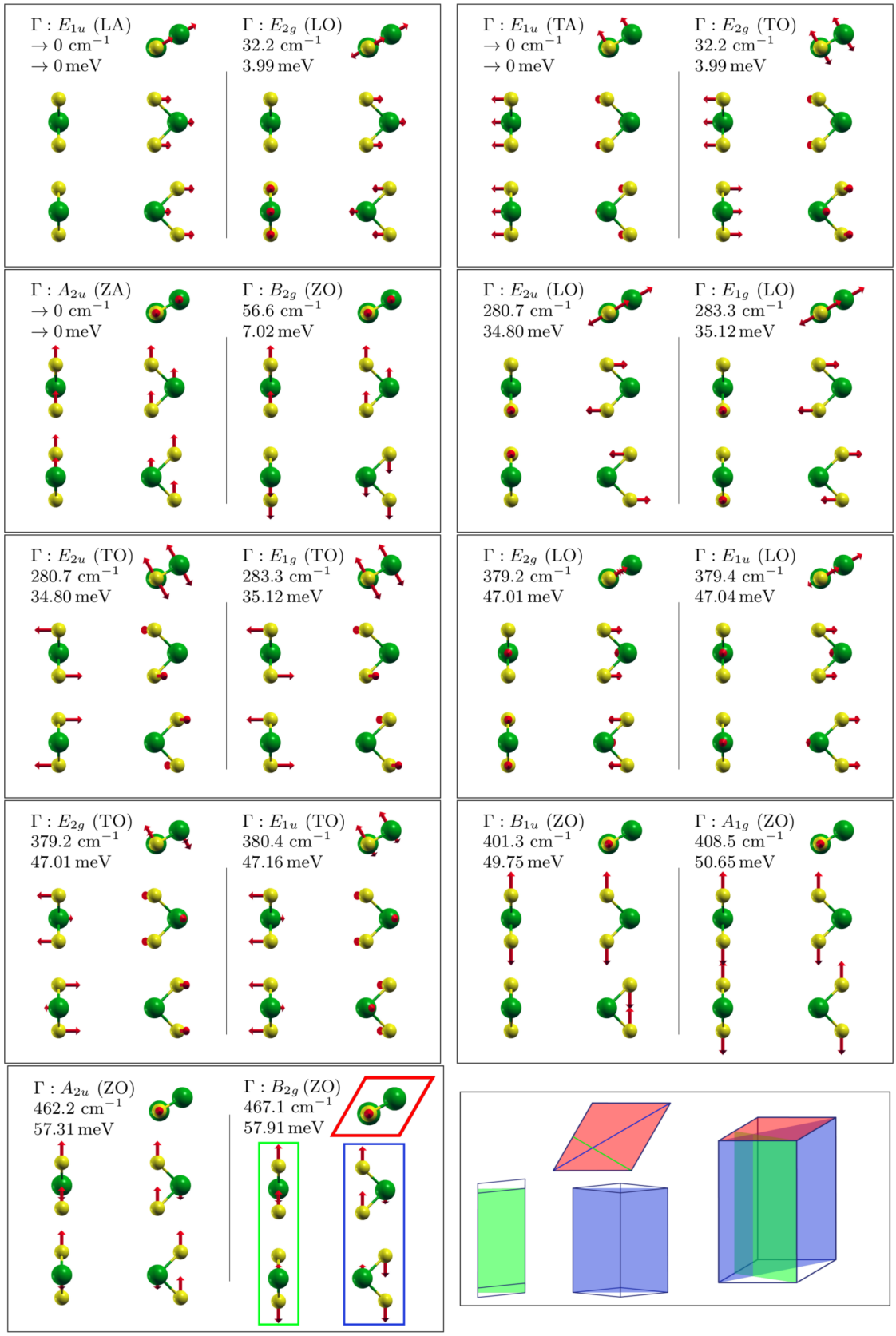

TABLE III. Eigenvectors of the MoS_2 phonons at the K point. Layout according to Table II.

$K : E''$ $\Gamma : B_{2g}$ (ZO) 183.1 cm^{-1} 22.70 meV	$K : E''$ $\Gamma : A_{2u}$ (ZA) 183.1 cm^{-1} 22.70 meV	$K : E'$ $\Gamma : E_{1u}$ (TA) 186.0 cm^{-1} 23.06 meV
$K : A_2'$ $\Gamma : E_{2g}$ (LO) 232.5 cm^{-1} 28.82 meV	$K : A_1'$ $\Gamma : E_{1u}$ (LA) 235.8 cm^{-1} 29.24 meV	$K : E'$ $\Gamma : E_{2g}$ (TO) 186.0 cm^{-1} 23.06 meV
$K : E''$ $\Gamma : E_{2u}$ (LO) 322.3 cm^{-1} 39.96 meV	$K : E''$ $\Gamma : E_{1g}$ (LO) 322.3 cm^{-1} 39.96 meV	$K : E'$ $\Gamma : E_{1u}$ (LO) 335.9 cm^{-1} 41.65 meV
$K : A_1''$ $\Gamma : E_{2u}$ (TO) 339.0 cm^{-1} 42.03 meV	$K : A_2''$ $\Gamma : E_{1g}$ (TO) 334.5 cm^{-1} 41.47 meV	$K : E'$ $\Gamma : E_{2g}$ (LO) 335.9 cm^{-1} 41.65 meV
$K : E''$ $\Gamma : B_{2g}$ (ZO) 370.1 cm^{-1} 45.89 meV	$K : E''$ $\Gamma : A_{2u}$ (ZO) 370.1 cm^{-1} 45.89 meV	$K : E'$ $\Gamma : B_{1u}$ (ZO) 393.0 cm^{-1} 48.73 meV
$K : A_2'$ $\Gamma : E_{1u}$ (TO) 376.7 cm^{-1} 46.70 meV	$K : A_1'$ $\Gamma : E_{2g}$ (TO) 379.4 cm^{-1} 47.04 meV	$K : E'$ $\Gamma : A_{1g}$ (ZO) 393.0 cm^{-1} 48.73 meV

TABLE IV. Eigenvectors of the MoS_2 phonons at the M point. Layout according to Table II.

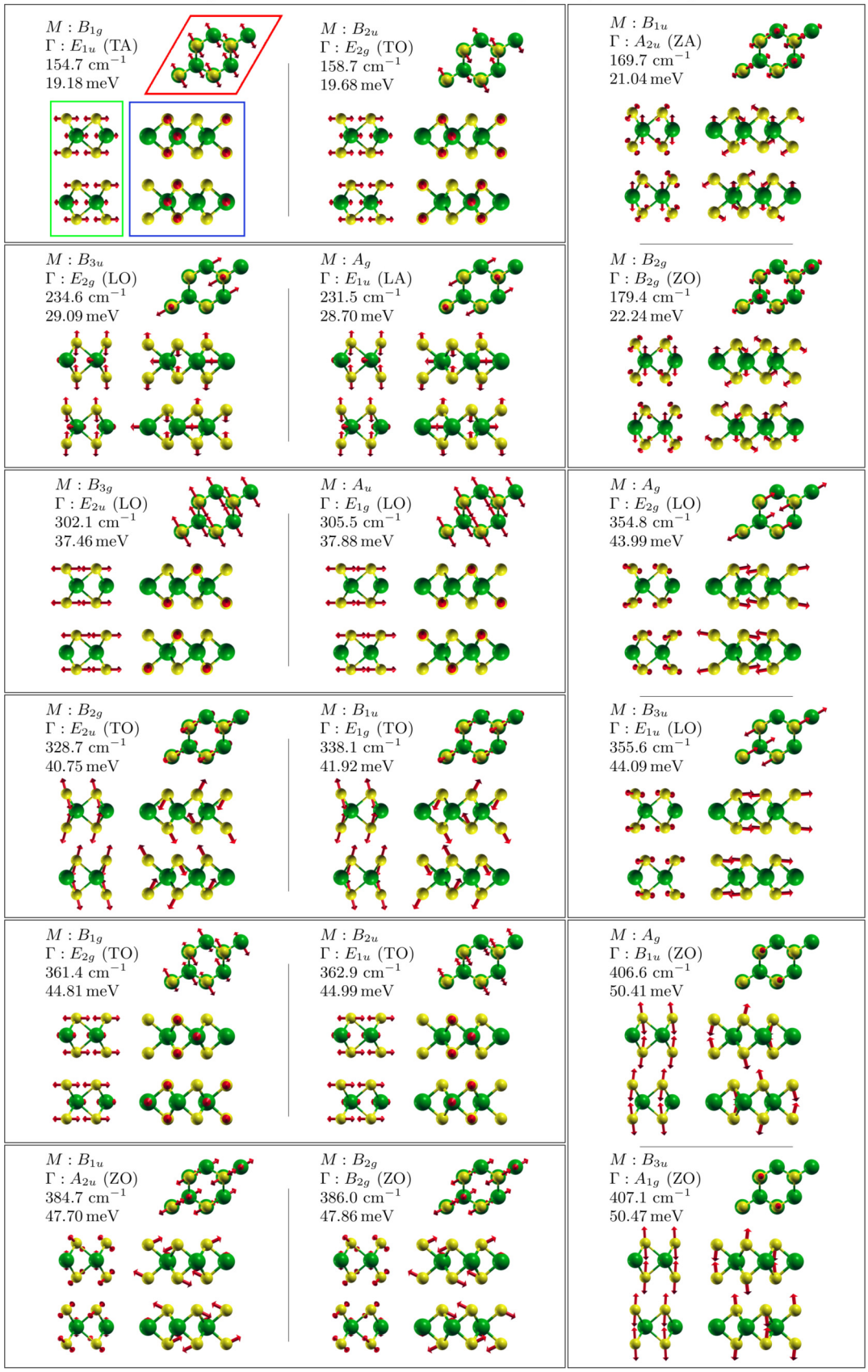

[1] K. F. Mak, C. Lee, J. Hone, J. Shan, and T. F. Heinz, Phys. Rev. Lett. **105**, 136805 (2010).

[2] A. Splendiani, L. Sun, Y. Zhang, T. Li, J. Kim, C.-Y. Chim, G. Galli, and F. Wang, Nano Lett. **10**, 1271 (2010).

[3] X. Xu, W. Yao, D. Xiao, and T. F. Heinz, Nat. Phys. **10**, 343 (2014).

[4] K. S. Novoselov, A. Mishchenko, A. Carvalho, and A. H. Castro Neto, Science **353**, aac9439 (2016).

[5] A. K. Geim and I. V. Grigorieva, Nature (London) **499**, 419 (2013).

[6] D. Xiao, G.-B. Liu, W. Feng, X. Xu, and W. Yao, Phys. Rev. Lett. **108**, 196802 (2012).

[7] A. Chernikov, T. C. Berkelbach, H. M. Hill, A. Rigosi, Y. Li, O. B. Aslan, D. R. Reichman, M. S. Hybertsen, and T. F. Heinz, Phys. Rev. Lett. **113**, 076802 (2014).

[8] C. Poellmann, P. Steinleitner, U. Leierseder, P. Nagler, G. Plechinger, M. Porer, R. Bratschitsch, C. Schüller, T. Korn, and R. Huber, Nat. Mater. **14**, 889 (2015).

[9] A. M. Dubrovkin, B. Qiang, H. N. S. Krishnamoorthy, N. I. Zheludev, and Q. J. Wang, Nat. Commun. **9**, 1762 (2018).

[10] C. Liu, X. Yan, X. Song, S. Ding, D. W. Zhang, and P. Zhou, Nat. Nanotechnol. **13**, 404 (2018).

[11] J. Liu, A. Goswami, K. Jiang, F. Khan, S. Kim, R. McGee, Z. Li, Z. Hu, J. Lee, and T. Thundat, Nat. Nanotechnol. **13**, 112 (2018).

[12] H. Jang, K. P. Dhakal, K. Joo, W. S. Yun, S. M. Shinde, X. Chen, S. M. Jeong, S. W. Lee, Z. Lee, J. Lee *et al.*, Adv. Mater. **30**, 1705190 (2018).

[13] M. Selig, G. Berghuser, A. Raja, P. Nagler, C. Schller, T. F. Heinz, T. Korn, A. Chernikov, E. Malic, and A. Knorr, Nat. Commun. **7**, 13279 (2016).

[14] C. Ruppert, A. Chernikov, H. M. Hill, A. F. Rigosi, and T. F. Heinz, Nano Lett. **17**, 644 (2017).

[15] R. Schmidt, G. Bergh'auser, R. Schneider, M. Selig, P. Tonndorf, E. Malić, A. Knorr, S. M. de Vasconcellos,, and R. Bratschitsch, Nano Lett. **16**, 2945 (2016).

[16] Y. Miyauchi, S. Konabe, F. Wang, W. Zhang, A. Hwang, Y. Hasegawa, L. Zhou, S. Mouri, M. Toh, G. Eda *et al.*, Nat. Commun. **9**, 2598 (2018).

[17] H. Tornatzky, A.-M. Kaulitz, and J. Maultzsch, Phys. Rev. Lett. **121**, 167401 (2018).

[18] K. F. Mak, K. He, J. Shan, and T. F. Heinz, Nat. Nanotechnol. **7**, 494 (2012).

[19] L. Yang, N. A. Sinitsyn, W. Chen, J. Yuan, J. Zhang, J. Lou, and S. A. Crooker, Nat. Phys. **11**, 830 (2015).

[20] L. A. Benítez, J. F. Sierra, W. S. Torres, A. Arrighi, F. Bonell, M. V. Costache, and S. O. Valenzuela, Nat. Phys. **14**, 303 (2018).

[21] X. Cui, G.-H. Lee, Y. D. Kim, G. Arefe, P. Y. Huang, C.-H. Lee, D. A. Chenet, X. Zhang, L. Wang, F. Ye *et al.*, Nat. Nanotechnol. **10**, 534 (2015).

[22] R. Gillen and J. Maultzsch, Phys. Rev. B **97**, 165306 (2018).

[23] J. Kunstmann, F. Mooshammer, P. Nagler, A. Chaves, F. Stein, N. Paradiso, G. Plechinger, C. Strunk, C. Schller, G. Seifert *et al.*, Nat. Phys. **14**, 801 (2018).

[24] N. Wakabayashi, H. G. Smith, and R. M. Nicklow, Phys. Rev. B **12**, 659 (1975).

[25] T. Wieting and M. Schlüter (eds.), *Electrons and Phonons in Layered Crystal Structures* (D. Reidel Publishing Company, Dordrecht, Boston, London, 1979).

[26] A. Molina-Sánchez and L. Wirtz, Phys. Rev. B **84**, 155413 (2011).

[27] C. Ataca, H. Şahin, and S. Ciraci, J. Phys. Chem. C **116**, 8983 (2012).

[28] A. Baron, Y. Tanaka, S. Goto, K. Takeshita, T. Matsushita, and T. Ishikawa, J. Phys. Chem. Solids **61**, 461 (2000).

[29] J. P. Perdew, K. Burke, and M. Ernzerhof, Phys. Rev. Lett. **77**, 3865 (1996).

[30] P. Giannozzi, S. Baroni, N. Bonini, M. Calandra, R. Car, C. Cavazzoni, D. Ceresoli, G. L. Chiarotti, M. Cococcioni, I. Dabo *et al.*, J. Phys.: Condens. Matter **21**, 395502 (2009).

[31] S. Grimme, S. Ehrlich, and K. Goerigk, J. Comput. Chem. **32**, 1456 (2011).

[32] R. Gillen and J. Maultzsch, IEEE J. Sel. Top. Quantum Electron. **23**, 219 (2017).

[33] C. Tyborski, R. Gillen, A. A. Fokin, T. V. Koso, N. A. Fokina, H. Hausmann, V. N. Rodionov, P. R. Schreiner, C. Thomsen, and J. Maultzsch, J. Phys. Chem. C **121**, 27082 (2017).

[34] D. R. Hamann, Phys. Rev. B **88**, 085117 (2013).

[35] M. J. van Setten, M. Giantomassi, E. Bousquet, M. J. Verstraete, D. R. Hamann, X. Gonze, and G.-M. Rignanese, Comput. Phys. Commun. **226**, 39 (2018).

[36] T. Wieting and J. Verble, Phys. Rev. B **3**, 4286 (1971).

[37] J. M. Chen and C. S. Wang, Solid State Commun. **14**, 857 (1974).

[38] N. Scheuschner, R. Gillen, M. Staiger, and J. Maultzsch, Phys. Rev. B **91**, 235409 (2015).

[39] J. Ribeiro-Soares, R. M. Almeida, E. B. Barros, P. T. Araujo, M. S. Dresselhaus, L. G. Cançado, and A. Jorio, Phys. Rev. B **90**, 115438 (2014).

[40] M. Mohr, J. Maultzsch, E. Dobardžić, S. Reich, I. Milošević, M. Damnjanović, A. Bosak, M. Krisch, and C. Thomsen, Phys. Rev. B **76**, 035439 (2007).

[41] J. Carrete, W. Li, L. Lindsay, D. A. Broido, L. J. Gallego, and N. Mingo, Mat. Res. Lett. **4**, 204 (2016).

[42] B. Van Troeye, M. Torrent, and X. Gonze, Phys. Rev. B **93**, 144304 (2016).

[43] J. P. Perdew, A. Ruzsinszky, G. I. Csonka, O. A. Vydrov, G. E. Scuseria, L. A. Constantin, X. Zhou, and K. Burke, Phys. Rev. Lett. **100**, 136406 (2008).

[44] M. Dion, H. Rydberg, E. Schröder, D. C. Langreth, and B. I. Lundqvist, Phys. Rev. Lett. **92**, 246401 (2004).

[45] K. Lee, E. D. Murray, L. Kong, B. I. Lundqvist, and D. C. Langreth, Phys. Rev. B **82**, 081101(R) (2010).

[46] O. A. Vydrov and T. Van Voorhis, Phys. Rev. Lett. **103**, 063004 (2009).

[47] A. Q. R. Baron, J. Spectrosc. Soc. Jpn. **58**, 205 (2009)(in Japanese), arXiv:0910.5764 (in English).

[48] B. Fåk and B. Dorner, Physica **234–236**, 1107 (1997).

[49] P. A. Bertrand, Phys. Rev. B **44**, 5745 (1991).

[50] See Supplemental Material at http://link.aps.org/supplemental/10.1103/PhysRevB.99.144309 for Raman spectroscopy of the sample used for IXS, a page-filling dispersion plot including the irreducible representations of all branches at the Γ (D_{6h}), K (D_{3h}), and M (D_{2h}) points and a comparison with the preceding experimental data. The discussion in the Supplemental Material includes the additional Refs. [51–53].

[51] H. Guo, Y. Sun, P. Zhai, J. Zeng, S. Zhang, P. Hu, H. Yao, J. Duan, M. Hou, and J. Liu, Nucl. Instrum. Methods Phys. Res. **381**, 1 (2016).

[52] S. Mignuzzi, A. J. Pollard, N. Bonini, B. Brennan, I. S. Gilmore, M. A. Pimenta, D. Richards, and D. Roy, Phys. Rev. B **91**, 195411 (2015).

[53] S. Reich, C. Thomsen, and J. Maultzsch, *Carbon nanotubes: basic concepts and physical properties* (Weinheim-VCH, Weinheim, Germany, 2004).

[54] For simplicity, we use the irreducible representations at the Γ point for labeling the entire branch inside the Brillouin zone. Where this is ambiguous, we add a superscript "Γ" to emphasize that this labeling is strictly correct only at the Γ point. For a correct symmetry assignment at the *K* and *M* points, see Table I in the main text and Tables II, III, and IV in the appendix.